


Vortex-induced vibrations of a low mass-damping rigid circular cylinder with forced periodic rotations

F. J. Huera-Huarte *Department of Mechanical Engineering, Universitat Rovira i Virgili (URV), 43007 Tarragona, Spain*

(Received 13 May 2020; accepted 12 November 2020; published 9 December 2020)

The one-degree-of-freedom vortex-induced vibrations (VIVs) of a low mass-damping circular cylinder forced to vibrate periodically have been investigated experimentally. A specially designed cylinder model allowed us to generate rotational oscillations while the system was responding to VIVs. Variations in the amplitude and frequency response have been studied, together with the excitation on the system. For dimensionless frequencies smaller than those of the response, rotations had little effect on the dynamics of the system. Otherwise, the dynamic response of the cylinder was in general reduced if compared to the nonrotating case, especially when forcing frequencies were larger than the VIV responding frequency under locked-in conditions. The very minor changes observed in the wake structures indicated that the VIV motion dominated the vortex formation process instead of the periodic forcing.

DOI: [10.1103/PhysRevFluids.5.124701](https://doi.org/10.1103/PhysRevFluids.5.124701)

I. INTRODUCTION

The flow around stationary cylinders has been extensively studied in past decades as it poses a canonical problem in fluid mechanics. There is abundant literature on the topic, ranging from the well-known book by Zdravkovich [1] to reviews such as Bearman [2] and Williamson [3], just to mention a few. If bluff bodies are flexibly mounted or are flexible themselves, the unsteady loads associated with vortex-shedding might result in vortex-induced vibrations (VIVs). The physics associated with this fluid-structure interaction phenomenon are very rich [4–7], and from a practical point of view, the phenomenon has many engineering implications [8–11].

The problem of a stationary continuously rotating cylinder in cross-flow has received considerably less attention. Early works mostly deal with aspects related to vortex street formation, wake asymmetries, and the way forces change with respect to the stationary nonrotating case [12–18]. A recent review by Rao *et al.* [19] describes the shedding modes and their transitions as a function of the rotation rate of the cylinder ($\alpha = U_s/U$) and the Reynolds number ($\text{Re} = UD/\nu$), where U is the current velocity, U_s is the cylinder surface velocity due to its rotation, D is the diameter of the cylinder, and ν is the fluid kinematic viscosity. The authors show that at low rotation rates ($\alpha < 1$) the phenomenon in the wake is very similar to that in stationary nonrotating cylinders. As the rate is increased, the wake becomes largely asymmetric and mode transitions occur at different Re . If the rotation rate is further increased, vortex shedding is suppressed ($\alpha \approx 2$) until the wake becomes unstable again at $\alpha \approx 4.5$.

The case of rotating cylinders allowed to vibrate is even more scarce in the literature. The first work combining the dynamic response of a circular cylinder in cross-flow with the rotation of the cylinder appears described by Stansby and Rainey [20,21]. The authors used computations combined with experiments to study the problem. The cylinder was mounted on top of a flume, in a pendulum rig that allowed axial rotations of the cylinder at different rates, while moving in three dimensions. They reported very large in-line static deflections as well as very large orbital

vibrations, in excess of five cylinder diameters in the transverse and in-line directions, running at small frequencies. These oscillations, which are more than five times larger than those expected in VIVs and at frequencies well away the natural frequencies of the system, were not associated with vortex shedding but to a galloping-like phenomenon.

It was not until Bourguet and Lo Jacono [22] performed two-dimensional (2D) direct numerical simulations (DNS) at low Re on a cylinder forced to rotate that the range of reduced velocities (ratio of free-stream velocity to a characteristic velocity of the cylinder motion) investigated, was compatible with VIVs. In their work, the cylinder was restricted to move with one degree of freedom, transversely to the imposed incoming flow. The authors described in detail the average lateral displacements and the full dynamic response as a function of the rotation rate and reduced velocity. Maximum amplitudes were found in excess (up to three times) those observed in nonrotating cylinders and took place at higher reduced velocities. The reduced velocity at the maxima increased with the rotation rate. Frequencies were compatible with VIVs as well, with values near the natural frequency of the system, and were reduced when the rotation rate increased. However, one of the most remarkable findings regarding the response of the system was that the range of reduced velocities in which there was VIV response, which in a nonrotating cylinder extends approximately from 4 to 10, was amplified as the rotation rate increased, reaching values over 30 at the highest rotation rates. This enlarged response region was observed for rotation rates up to 4, where the VIV response completely vanished. The paper contains as well an in-depth analysis of the wake structures and forces. In a second work, Bourguet [23] using 2D and three-dimensional (3D) DNS, described in detail the same problem, but in this case the cylinder was allowed to vibrate at a certain angle in respect to the incoming cross-flow. Dynamic response maps were provided as a function of the degree-of-freedom inclination and the reduced velocities for several selected rotation rates (no rotation, slow and fast rotations). Regions of VIV response were clearly distinguished from others where the response was galloping-like at the fastest rotations investigated. Another set of numerical simulations at low Re was conducted by Zhao *et al.* [24] with a rotating cylinder with one and two degrees of freedom, at three rotating rates, covering a wide range of reduced velocities. The paper discusses the dynamic response in each scenario, showing motions, forces, and wake structures. They presented a wider response region in reduced velocity at the highest rotation rate investigated, as in the work by Bourguet and Lo Jacono [22]. More recently, Bourguet [23] and Zhao *et al.* [25] worked on variants of the same problem with a rotating cylinder, vibrating in an arbitrary direction and in the in-line direction, respectively.

Seyed-Aghazadeh and Modarres-Sadeghi [26] conducted the first set of experiments with a continuously rotating cylinder undergoing VIVs. They used a cylinder in cross-flow, with a mass ratio near 11, to conduct experiments in a one-degree-of-freedom rig. They reported minor changes in the dynamic response of the cylinder at small rotation rates ($\alpha < 1$) when compared to the nonrotating cylinder, with dimensionless amplitudes that practically did not vary. As the rotation rate was increased, they found a minor decrease of the reduced velocity lock-in bandwidth that was especially pronounced at 2.4, where lock-in was identified for reduced velocities in the range from 6 to 8. For this rotation rate, the maximum amplitude increased by a 20%. Their results indicated that as the rotation rate was increased, the lock-in region was reduced until it disappeared. The same phenomenon was observed at smaller Re , in the 3D numerical simulations by Bourguet and Lo Jacono [27], with the disappearance of VIVs at a rotation rate of 3.75 and a widening of the response region in the reduced velocity axis. There were major differences between these two works, which were attributed to the differences in Re and more importantly to the mass-damping characteristics of the systems.

Wong *et al.* [28] performed a comprehensive set of experiments conducted with a low mass-damping cylinder undergoing VIVs while being forced to rotate. The authors covered a very wide parameter space by changing the rotation rate and reduced velocity, for Re varying from approximately 1000 to over 6000. The VIV response for rates up to 2 was very similar to that of the nonrotating cylinder, with amplitude peaks that were slightly larger. When the rotation rate reached a value of 2, amplitudes started to fall and the response curve became very different from

that of a nonrotating cylinder. They showed amplitude discontinuities at an α of 1.7 and 2.3. The authors used as well digital particle image velocimetry (DPIV) combined with proper orthogonal decomposition [29] to discuss the wake topology found in the experiments, summarizing it in a vortex mode map.

From the previous published work on continuously rotating cylinders, we know that the dynamic response at moderate to high angular speeds is substantially different from that of a nonrotating cylinder. Depending on the different combinations of Re , reduced velocity, and rotation rates, cylinders can exhibit VIVs or a galloping response with a wide variety of amplitude and frequency response scenarios. Although the wake can be largely altered, rotation does not lead to the complete suppression of VIVs.

The case of stationary cylinders with applied rotational oscillations is as well relevant to the work presented here. Several authors have studied the application of periodic rotational forcing and its relationship with the shedding process [30–34] as a method for flow control and drag reduction [35–37]. As in the case of continuous rotation, the boundary layer developing on the cylinder can be modified, producing great changes on how vortex formation takes place. However, the problem is substantially different because continuous rotations imply a forced wake asymmetry. In the case of rotational oscillations, the rotational rate that relates the cylinder surface velocity to the free stream is dependent on the forcing frequency imposed, which interacts with the shedding frequency in a more complex fashion. There is also the fact that rotational oscillation rates cannot in principle, at least from a practical point of view, be as large as those achieved with continuously rotating systems. Notwithstanding this fact, Tokumaru and Dimotakis [35] after their work with stationary cylinders suggested that rotational oscillations could prevent or reduce vortex-induced vibrations in cases with flexibly mounted systems, although this has never been investigated.

The problem posed in this paper deals with a low mass-damping cylinder allowed to freely vibrate with one degree of freedom, while periodic rotations are applied to the model. The work is focused on describing and discussing the effects of forced rotary oscillations on the VIV dynamic response of the cylinder, having always as a reference the case of the nonrotating cylinder. The paper is organized as follows: The experimental methods are presented in Sec. II, followed by the results showing the effect of the periodic rotations in the dynamic response in Sec. III A. The sensitivity of the dynamic response to the frequency of the forced oscillations is discussed in Sec. III B and the effects on the wake structures in Sec. III C. Finally the conclusions are given in Sec. V.

II. EXPERIMENTAL METHODS

A. The cylinder model

The cylinder model consists of an acrylic tube with an external diameter (D) of 50 mm. A schematic showing the details of the design is presented in Fig. 1. In its upper end the cylinder is connected to a servo motor that produces the controlled periodic rotations. Just below the servo location, a needle bearing installed in a 3D printed part allows smooth rotations of the cylinder. The needle bearing has an internal diameter of 50 mm (the external diameter of the cylinder) and an external one that fits it to the 3D printed part. A ring installed just below the needle bearing allows the model to sit on top of a thrust bearing, and in this way the servo motor is not loaded axially by the weight of the system. This design is very robust, as it allows smooth axial rotations of the cylinder and it avoids any pendulum-like vibrations of the cylinder during the experiments. At the same time it is compact and light, yielding an overall low mass of the system. Moreover, the external 3D printed part at the upper end of the model encapsulates all the elements that allow the rotation and connects the model to a six-axis load cell, which is installed hanging from an air-bearing carriage allowed to move only transversely to the flow direction. An in-house code implemented in a microcontroller and based on the generation of a pulse width modulated (PWM) signal allows the servo to be sinusoidally actuated, producing the desired rotations on the cylinder model.

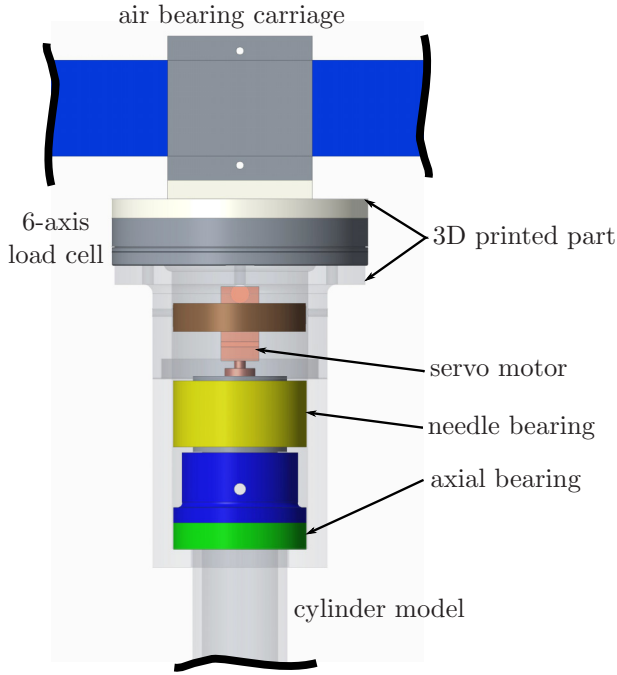


FIG. 1. Schematic of the mechanical design of the servo rotational system.

B. The experimental setup

The air-bearing rail system is installed on top of a free surface water channel, leaving a submerged length L in the model of 520 mm ($> 10D$). When the channel generates a current, only that part of the cylinder is exposed to the flow as depicted in the overall schematic of the experiment, in Fig. 2. The structure that supports the air-bearing system is completely independent of the water channel, and in this way the small vibrations produced during the operation of the pumps are not transmitted to the experiment. The model is linked to its supporting structures by means of two springs with elastic constant k that provide the restoring forces to the system.

The blockage, defined as the ratio between the longitudinal area of the cylinder (LD) and the water channel cross-sectional area, is less than 3%. The gap between the cylinder and the walls and between the bottom end of the cylinder and the channel floor is large enough ($> 8D$) to avoid any wall/floor effects. The variability in the flow profile generated in the water channel is less than 1.6%. This is defined as the spatiotemporal variability of the flow velocity in the channel in the yz plane of the working section where the cylinder is placed. The measured turbulence intensity (U_{rms}/U_{mean}) was found to be 2.79% at the highest regime of the channel, i.e., the worst case scenario. These values were obtained after processing data collected using a traverse system and an acoustic Doppler velocimeter. The data were obtained at 11 locations along the width of the channel and 3 along the height, in three yz planes of the working section.

A series of decay tests in air showed very low damping. If expressed as a ratio of the critical damping (ξ), its value was found to be 0.0046. The total structural mass of the system (m), including the air-bearing carriage, the load cell, the cylinder model, and the parts used to connect all of them, resulted in a mass ratio ($m^* = \frac{4m}{\rho\pi LD^2}$) of 3.17, with ρ being the fluid density. In the experiments by Seyed-Aghazadeh and Modarres-Sadeghi [26], with a continuously rotating cylinder undergoing VIVs, the mass ratio and the damping ratio were both an order of magnitude larger than in the ones presented here, indicating the difficulty of experimentally keeping these parameters low. Here the combined mass-damping parameter ($m^*\xi$) ended up being as low as 0.0145, with these values being

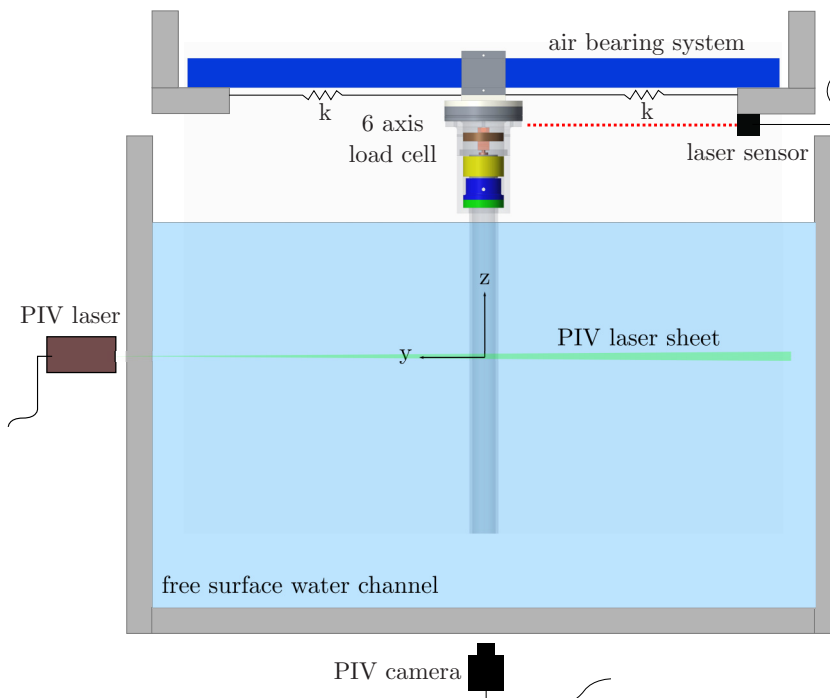


FIG. 2. Schematic view of the experimental setup in the free surface water channel.

typical of ocean structures. The Reynolds number (Re) based on the cylinder model diameter ranged from approximately 9000 to 22 000. The ratio between the free-stream velocity in the channel and the average velocity of the cylinder (based on its natural frequency in water f_o , that was 0.98 Hz) is defined as the reduced velocity $U^* = U/f_o D$, and ranged from near 4 to more than 11. Both parameters were varied during the experiments by changing the free-stream velocity in the water channel.

Prior to the beginning of the experiments, a series of validation tests were run to certify the correct measurement of the forces, which is of particular complexity in this type of setup. An auxiliary system based on a secondary air-bearing carriage was installed allowing a second load cell to be used. The later was a precision load cell with a measurement range of ± 8.9 N and an accuracy of 0.01%, installed between the two carriages and measuring directly the transverse force on the system. In this way the force was measured using two completely independent measurement systems, which led to the same results. The same arrangement was used to validate the force measurements in Huera-Huarte [38]. After the validation, the second auxiliary carriage was removed in order to keep the mass ratio as low as possible. The VIV transverse motion $y(t)$ and the rotations $\theta(t)$ imposed on the cylinder were measured using two nonintrusive laser displacement sensors with a resolution of $\pm 0.002D$ and experimental errors under 1% (less than 0.3% in the upper branch). All signals were sampled synchronously at 2 kHz, using an in-house code written to control the data acquisition devices.

III. RESULTS

Results are presented in this section using the transverse amplitude of the model in dimensionless form ($A^* = A/D$). A is the mean of the amplitude peaks of the displacement of the system $y(t)$, computed using the Hilbert transform [38,39]. The dominant frequencies of the transverse motion ($f^* = f_y/f_o$), obtained using Fourier analysis, are presented as well in dimensionless form, using

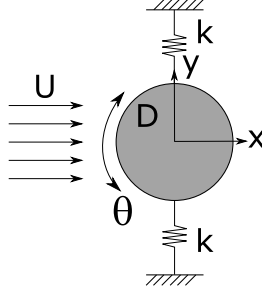


FIG. 3. Cross-sectional schematic of the experiment, showing the one-degree-of-freedom system with forced axial rotations.

the natural frequency in water of the system f_0 , from decay tests. Measured forces are shown as dimensionless coefficients, which are computed using the following expressions:

$$\bar{C}_x = \frac{\bar{F}_x}{\frac{1}{2}\rho U^2 DL}, \quad (1)$$

$$\hat{C}_y = \frac{\hat{F}_y}{\frac{1}{2}\rho U^2 DL}, \quad (2)$$

where \bar{F}_x is the mean in-line force or drag, and \hat{F}_y is the peak transverse force or lift, computed by multiplying $\sqrt{2}$ and the root-mean-square value of the transverse force. The phase difference between the transverse excitation and the motion ϕ [38] is also presented.

As shown in the top schematic view of Fig. 3, the cylinder was forced to rotate periodically about its axis as indicated by $\theta = \hat{\theta} \sin(2\pi f_r t)$, with an amplitude $\hat{\theta}$ and a frequency f_r . The velocity of rotation is $\dot{\theta} = 2\pi f_r \hat{\theta} \cos(2\pi f_r t)$, where the dot indicates the time derivative. A dimensionless velocity or rotation rate (α) similar to that used by previous authors in continuously rotating cylinders can be defined as the ratio between the peak velocity of the cylinder at its surface due to the rotation, divided by the free-stream velocity:

$$\alpha = \frac{\pi D f_r \hat{\theta}}{U}. \quad (3)$$

Different sets of experiments were conducted. Initially, the rotation frequency was varied to study its effects on the responding amplitudes, frequencies, and forces. This was done for two forcing amplitudes of $\pi/6$ and $\pi/4$, i.e., 30° and 45° (Sec. III A), with the cylinder sweeping 60° or 90° , respectively. Larger values of rotation were not considered as the servo had difficulties in achieving the same frequency-amplitude combinations at larger amplitudes. The servo used in the experiments had to be of relatively small size so it could be embedded in the model (see Fig. 1), moving with it while undergoing VIVs, in order to keep an overall low mass damping. In setups where the cylinder is stationary, the mass ratio would not be a design parameter at all, and the forcing system could be as large as needed, and therefore larger frequency-amplitude combinations could be achieved. For each forcing configuration implemented, multiple experiments were run at different Re and U^* .

A second set of experiments was conducted to investigate the effect of small variations of the forcing frequency near the responding frequency or its multiples. Finally, more experiments were conducted by fixing the reduced velocity and varying the forcing frequency (Sec. III B). DPIV results have been used as a flow visualization method for specific experiments and are discussed in Sec. III C.

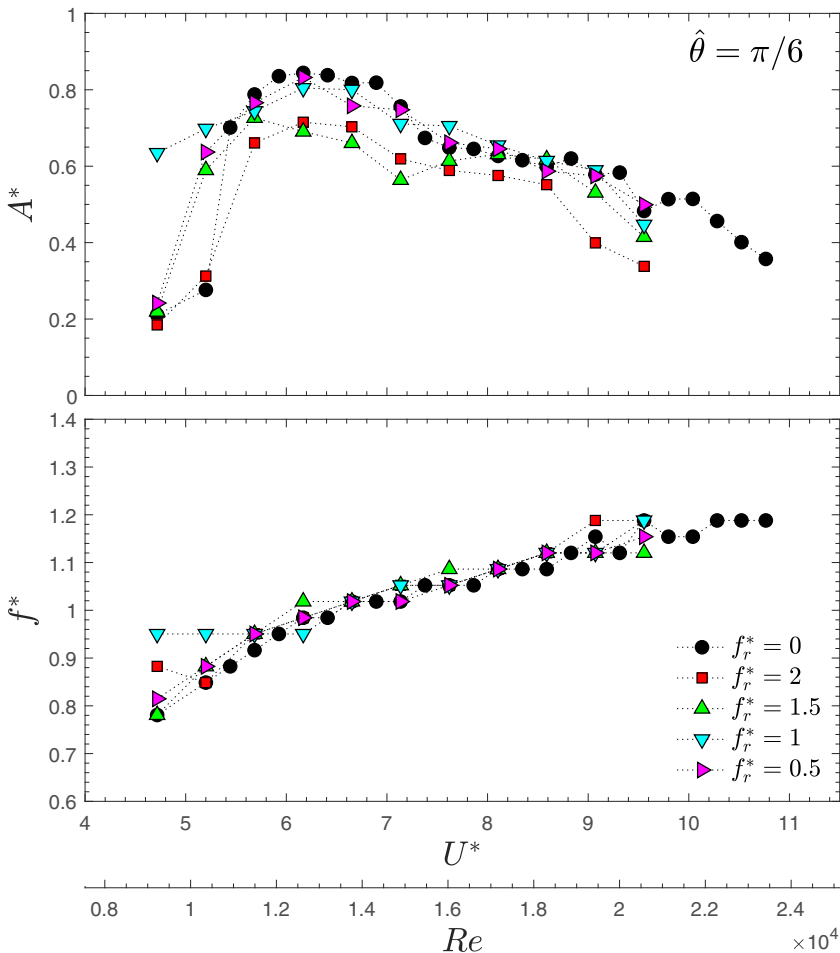


FIG. 4. Dimensionless response amplitude (A^*) and frequency (f^*) as a function of the reduced velocity (U^*) and Reynolds number (Re), for the case with forced rotational amplitude $\hat{\theta} = \pi/6$ rad. The reference case ($\hat{\theta} = 0$) is shown using solid circles and the rest of the cases with varying frequencies with colored symbols.

A. Effect of the forcing angular amplitude and frequency on VIVs

In this section the effects of the angular forcing on the system are presented. Throughout the section, solid black circles are used to show the results of the reference case, the system without rotation ($\hat{\theta} = 0$). The dynamic response is comparable to that obtained previously in the same facility [38–40] and to those reported in other experiments with cylinders with a similar mass ratio [4,41].

Colored symbols are used for the different forcing rotational frequencies (f_r), as indicated in the legend of the subsequent plots. To obtain the results presented in this section, the frequencies were varied from 0.5 to 2 Hz in 0.5 Hz steps. In dimensionless form, the forcing frequency can be expressed as $f_r^* = f_r/f_0$, with values that stay in the range from 0.5 to 2, because $f_0 \approx 1$. Given those frequency values, the imposed amplitudes, and the free-stream velocities used in the experiments, α varied in the range from 0 to 1.1. An analysis of the effects of producing small variations in f_r^* around the natural frequency and its multiples appears in Sec. III B.

Figures 4 and 5 display the dynamic response of the system with imposed amplitudes of rotation $\hat{\theta}$ of $\pi/6$ and $\pi/4$, respectively. The reference case ($\hat{\theta} = 0$) is included in both figures, depicting the

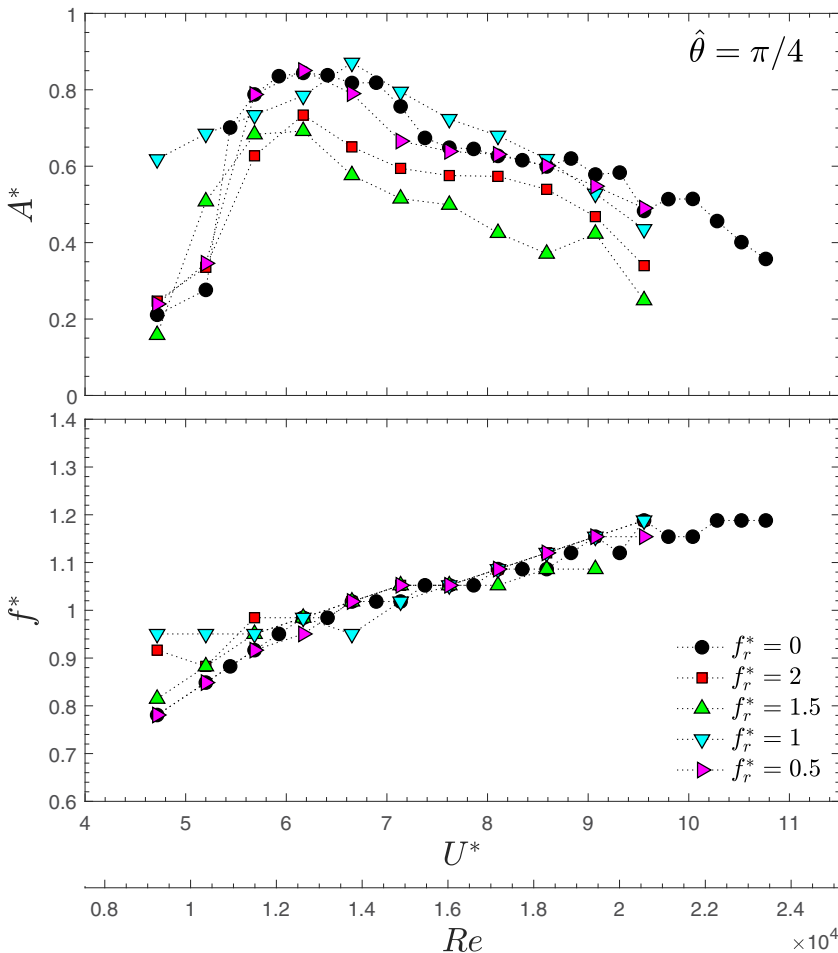


FIG. 5. Dimensionless response amplitude (A^*) and frequency (f^*) as a function of the reduced velocity (U^*) and Reynolds number (Re), for the case with forced rotational amplitude (θ) of $\hat{\theta} = \pi/4$ rad. The reference case ($\hat{\theta} = 0$) is shown using solid circles and the rest of the cases with varying frequencies with colored symbols.

classical VIV response of a low mass-damping circular cylinder [41], with the well-known regions of response, i.e., initial ($U^* \lesssim 5.5$), upper ($5.5 \lesssim U^* \lesssim 7.5$) and lower branches ($U^* \gtrsim 7.5$). At the smallest rotational frequency ($f_r^* = 0.5$), the response of the system does not significantly vary when compared to the reference case. This is true for both rotational amplitudes investigated, $\pi/6$ (Fig. 4) and $\pi/4$ (Fig. 6). When the dimensionless rotational frequency is set to 1, inside the upper branch amplitudes are smaller than those of the nonrotating model ($\approx 3\%$ reduction). In the lower branch amplitudes are again very similar, but in the initial branch amplitudes are clearly larger (up to three times). This applies to both rotational amplitudes considered in Figs. 4 and 5. For these cases, the response frequency appears increased to values near the natural frequency of the system, indicating an enlargement of the lock-in region. When the dimensionless forcing frequency is increased to 1.5 and 2, changes are more evident, and although the trends still show the classical branches of response, amplitudes are reduced especially in the upper and lower branches. The maximum amplitude reductions take place for the case with amplitude $\hat{\theta} = \pi/4$ and forcing frequency $f_r^* = 1.5$, where the data points evolve parallel to the no rotation case, with amplitudes

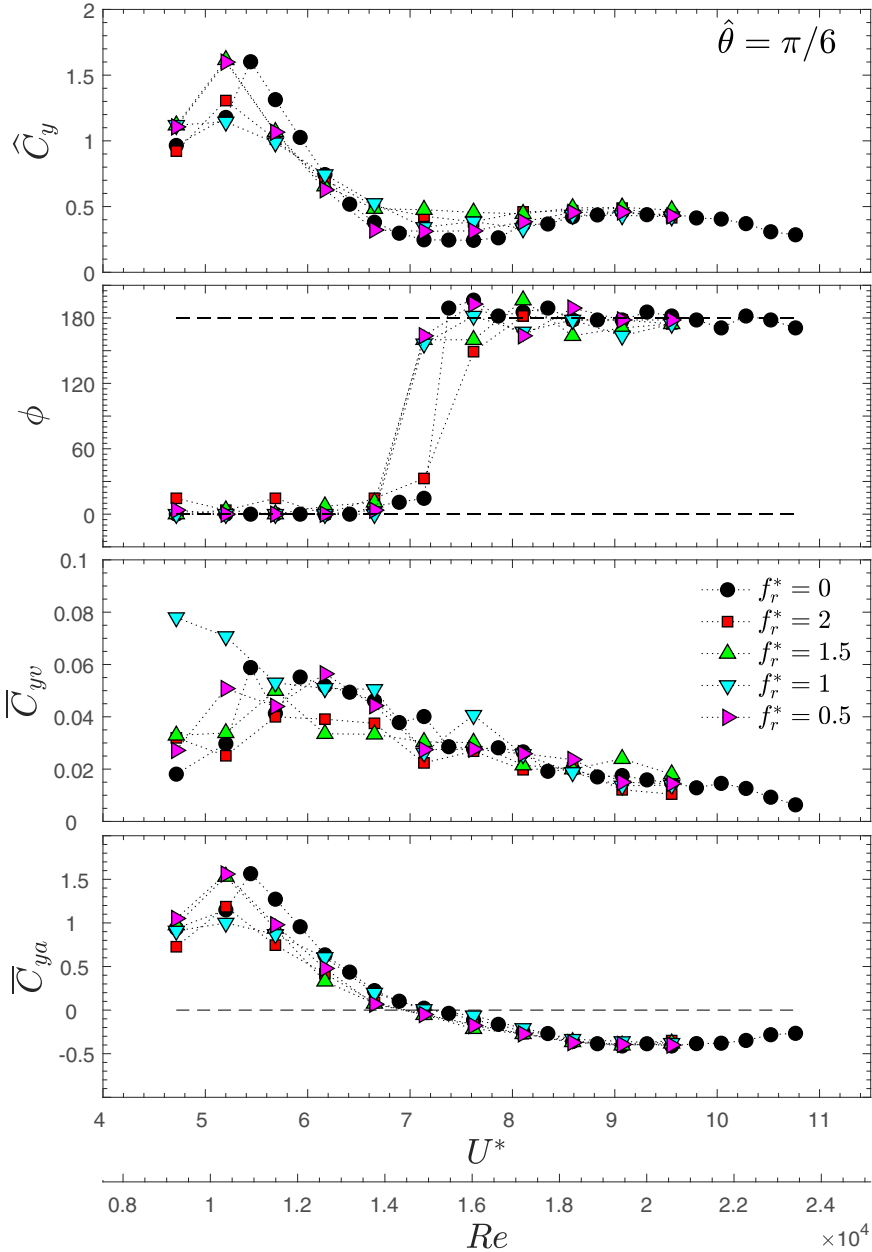


FIG. 6. Lift coefficient (\hat{C}_y) and phase (ϕ) as a function of the reduced velocity (U^*) and Reynolds number (Re), for the case with forced rotational amplitude $\hat{\theta} = \pi/6$ rad. Lift-in phase with velocity (\bar{C}_{yv}) and with acceleration (\bar{C}_{ya}). The reference case ($\hat{\theta} = 0$) is shown using solid circles and the rest of the cases with varying frequencies with colored symbols.

that are approximately 25% to 30% smaller. In the case of the responding frequencies f^* , changes are observable only in the initial branch, at the smallest reduced velocities. In general, the forcing rotation had a very limited effect on the VIV responding frequency of the system.

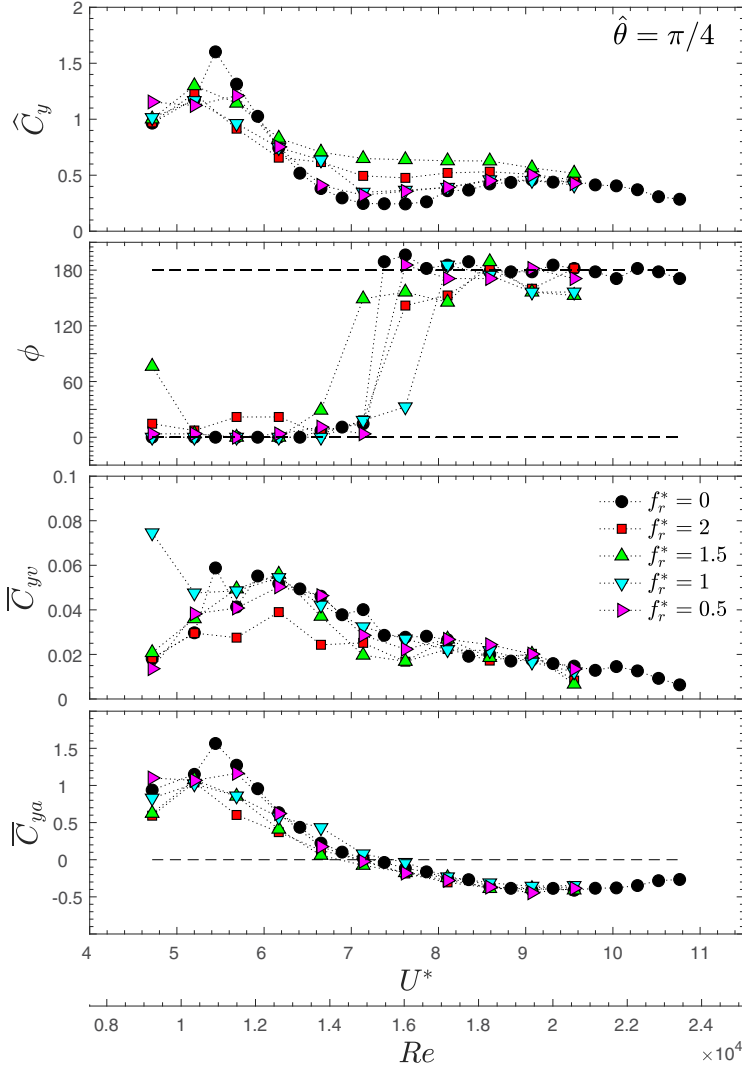


FIG. 7. Lift coefficient (\hat{C}_y) and phase (ϕ) as a function of the reduced velocity (U^*) and Reynolds number (Re), for the case with forced rotational amplitude (θ) of $\hat{\theta} = \pi/4$ rad. Lift-in phase with velocity (\bar{C}_{yv}) and with acceleration (\bar{C}_{ya}). The reference case ($\hat{\theta} = 0$) is shown using solid circles and the rest of the cases with varying frequencies with colored symbols.

The excitation on the system appears in Figs. 6 and 7 for both forcing amplitudes. In the uppermost plot of the figures, lift coefficients (\hat{C}_y) computed as in Eq. (2), are shown. The reference case is characterized by the classical lift curve with a sharp peak with values over 1.5 at the end of the initial branch that quickly decrease to values under 0.5, as reduced velocity is increased. The phase between response and excitation (ϕ) changes from the in-phase to the out-of-phase condition at the end of the upper branch. In the cases with imposed rotation, the trends depicted by the lift curves are in accordance to those shown by the reference case. Peak values at the end of the initial branch are very similar to those of the reference case but mildly attenuated when there is forced rotation on the cylinder. The values are higher in the upper and lower branches, that being true for both rotational amplitudes of $\pi/6$ and $\pi/4$. There are also changes in the jump of the phase, which

are more pronounced in the cases with the largest forcing amplitude. The phase shift is in general produced at a smaller reduced velocity, especially in the cases with $f_r^* = 1.5$.

The transverse force can be separated into components in phase with velocity (C_{yv}) and with acceleration (C_{ya}), related to damping and inertial effects, respectively. These quantities given by expressions (4) and (5), appear in time-averaged form (\overline{C}_{yv} and \overline{C}_{ya}) in the two lower plots of Figs. 6 and 7. The term C_{y0} in the equations is the instantaneous fluctuating transverse coefficient (obtained by removing its mean), which is multiplied by the instantaneous velocity or displacement, divided the square root of the time-averaged squared velocity or displacement, respectively:

$$C_{yv} = \sqrt{2}C_{y0} \left(\frac{\dot{y}}{\sqrt{\dot{y}^2}} \right), \quad (4)$$

$$C_{ya} = \sqrt{2}C_{y0} \left(\frac{y}{\sqrt{y^2}} \right). \quad (5)$$

Positive values of \overline{C}_{yv} indicate the fluid excites the structural response (net energy transfer from the fluid to the body), and negative ones are an indication of fluid damping. As happens with the reference case, for both forced rotational amplitudes, and for all reduced velocities, the part of the lift-in phase with velocity is positive, with maximums that clearly correlate in the initial and upper branches, with the maximum levels of response presented in Figs. 4 and 5.

Regarding \overline{C}_{ya} , which is related to the fluid inertia, a peak is found in the reference case at a reduced velocity near 5.5. Further increase of U^* yields a reduction of the coefficient up to a point at which it becomes negative ($U^* \approx 7.4$), where there is the jump in phase ϕ , from 0° to 180° . For larger reduced velocities the excitation opposes the cylinder motion, weakening the response through the lower branch, and indicating somehow that inertia prevents synchronization between the excitation and the motion. In the cases with forced rotation, the point at which \overline{C}_{ya} becomes negative happens at a smaller reduced velocity in general. This is more evident when $f_r^* = 1.5$ with the zero crossing and the phase shift taking place at $U^* \approx 6.8$.

Finally, the in-line excitation appears in Figs. 8 and 9, as a function of the dimensionless amplitude and of the reduced velocity, respectively. The plots showing the drag-amplitude relationship are used to emphasize the drag amplification that takes place when the transverse response is large. In the plots, the dash-dotted line is the best quadratic fit to the reference case data, forcing the no-motion case to the drag values expected for stationary cylinders at the same Re, and it is clear how the drag increases monotonically with amplitude. This effect holds true for the cases with forced oscillations at all frequencies and amplitudes. The lower plots, with data presented as a function of U^* , show that drag values mostly remain under the no-rotation curve, indicating the clear correlation with VIV transverse displacement, which is in general reduced.

B. Sensitivity of the VIV amplitude to the forcing angular frequency

The experiments analyzed in the previous section (III A), show that in cases with f_r^* being 1.5 or 2, amplitudes and hydrodynamic force coefficients were consistently altered if compared to the nonrotating case. In order to further investigate the effects of the forced rotational motions on the system, a series of tests were conducted by producing small variations in the rotational frequency, in cases in which large effects on the amplitudes were seen. Initially, the effect of using a frequency that is exactly twice the natural frequency of the system ($f_r^* = 2$) is investigated, against a case with a frequency that is only close to twice the natural frequency of the system ($f_r^* \approx 2$). The results of this comparison appear in Fig. 10 for forcing amplitudes of $\pi/6$ and $\pi/4$, where it is evident that these minor differences when setting the forcing frequency lead to only minor changes in the responding amplitudes and frequencies, which were in any case smaller than the differences observed with the reference case. Only at the peak of the upper branch and at the end of the desynchronization branch

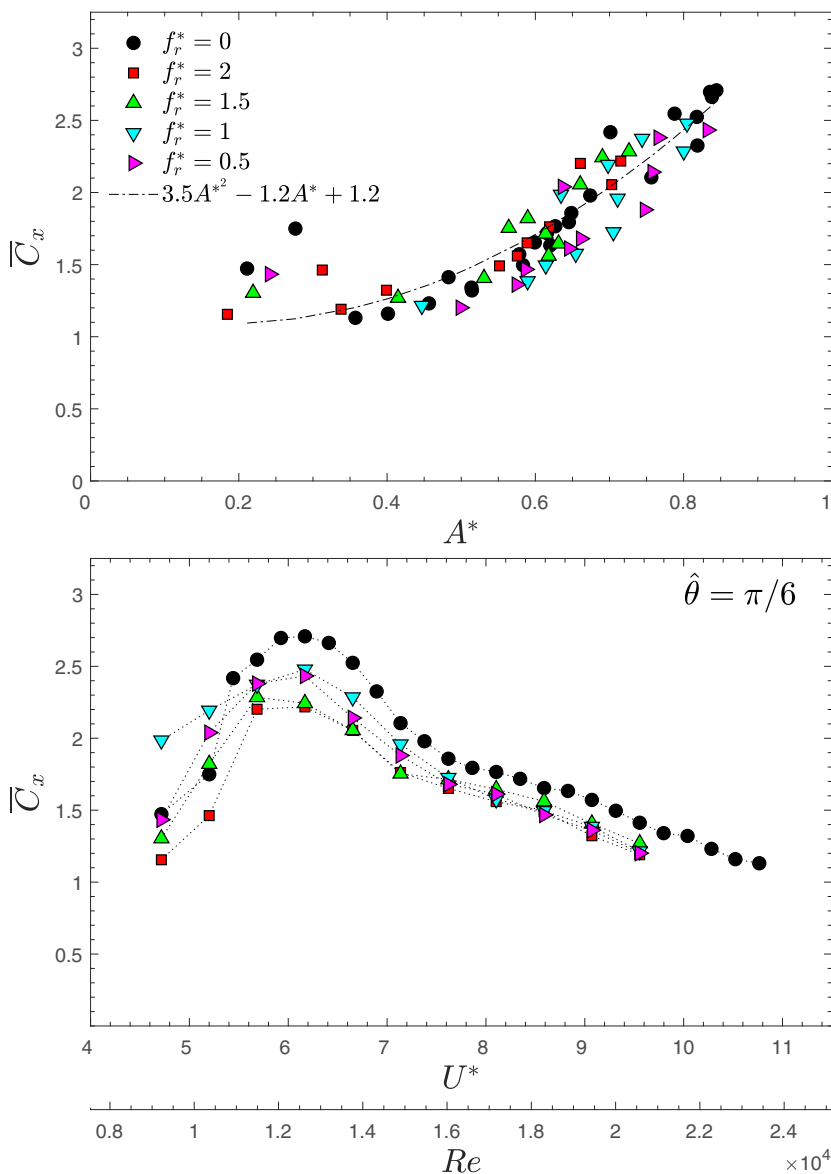


FIG. 8. Drag coefficient (\bar{C}_x) as a function of the dimensionless amplitude (A^*) and as a function of the reduced velocity (U^*) and Reynolds number (Re), for the case with forced rotational amplitude $\hat{\theta} = \pi/6$ rad. The reference case is shown using solid circles and the rest of the cases with varying frequencies with colored symbols. The dash-dot line indicates the best quadratic fit to the reference case without rotation ($\hat{\theta} = 0$).

are differences in amplitude relevant as will be discussed in the following paragraph. The excitation plots for these cases show as well very minor changes, and they have not been included for the sake of brevity.

In order to further investigate this matter, a series of experiments were conducted by keeping the rotational amplitude at $\pi/6$ while increasing the forcing frequency in small steps, from an f_r^* of 0.5, where very mild effects were observed (Sec. III A), to over 2.5. All these cases were done at a reduced velocity of approximately 6.2, where amplitudes were found to be the largest, and the

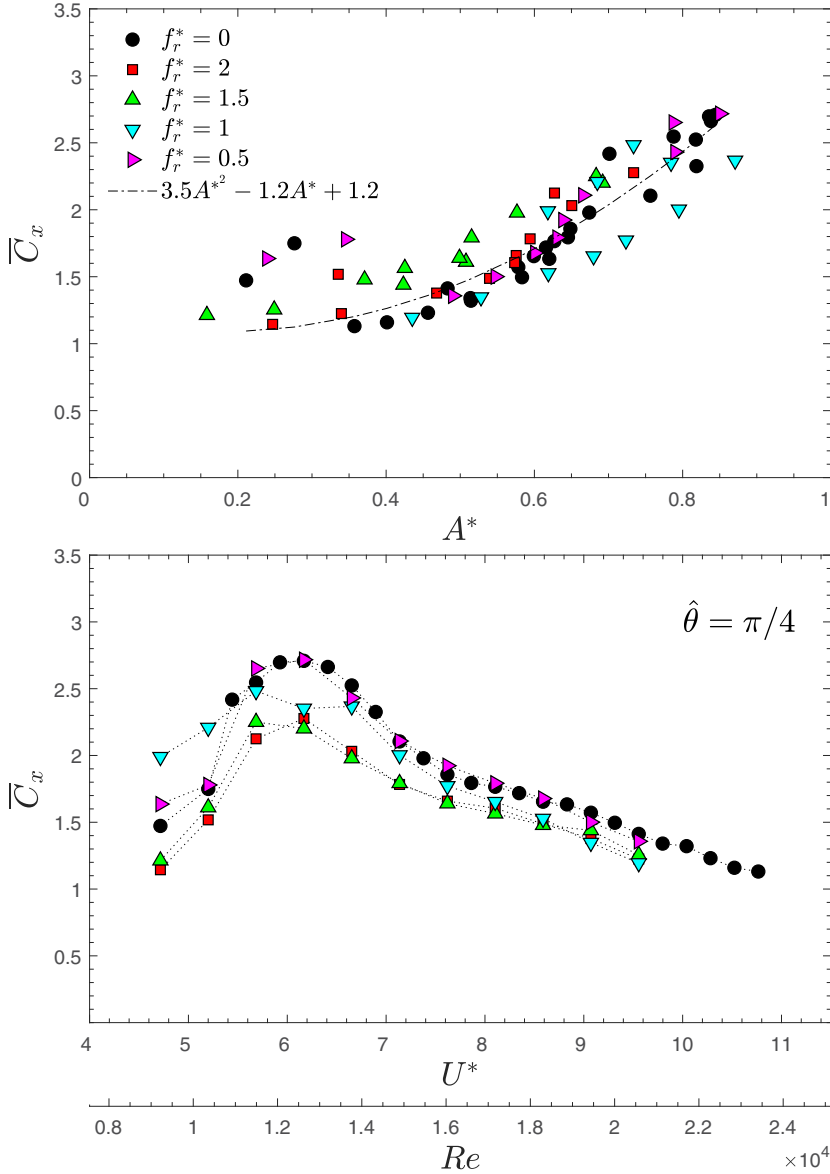


FIG. 9. Drag coefficient (\bar{C}_x) as a function of the dimensionless amplitude (A^*) and as a function of the reduced velocity (U^*) and Reynolds number (Re), for the case with forced rotational amplitude $\hat{\theta} = \pi/4$ rad. The reference case is shown with solid circles and the rest of the cases with varying frequencies with colored symbols. The dash-dot line indicates the best quadratic fit to the reference case without rotation ($\hat{\theta} = 0$).

largest differences with the nonrotating case were observed (Figs. 4 and 5). These 28 experiments appear summarized in Fig. 11, with dimensionless amplitudes, frequencies, forces, and phases. The amplitude plot shows that there are two clear levels of response depending on the forcing frequency configured in the system, one at around 80% of the cylinder diameter and another at 65%. The jump from the upper level of amplitude to the lower one takes place gradually just after passing through an f_r^* of approximately 1. The same trend is observed in the drag coefficient that appears in the last row of plots, as it is correlated to the amplitude (Figs. 8 and 9). A narrow peak is observed near a

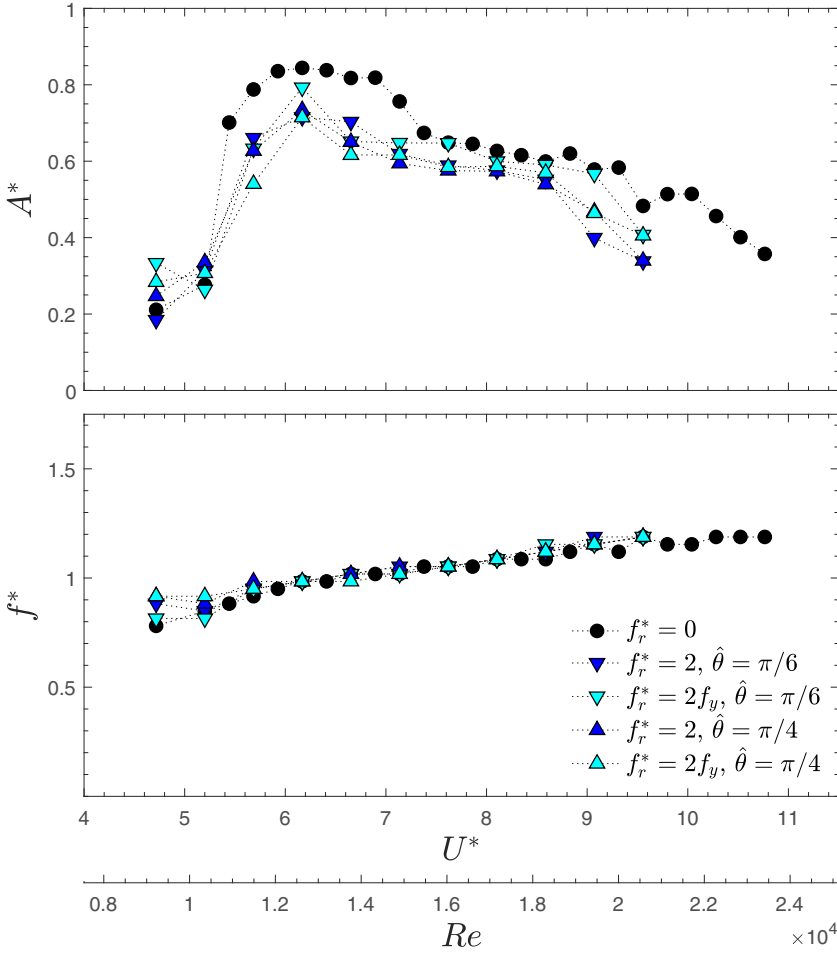


FIG. 10. Dimensionless amplitude and frequency as a function of Reynolds number Re and reduced velocity U^* , for cases with forcing frequency of approximately twice the natural frequency and exactly twice the responding frequency f_y .

$f_r^* \approx 2$. The dominant transverse frequency and force as well as the phase difference do not show the same trends, with values that remain almost unaltered.

C. Effect of the forcing rotations on the near wake dynamics

In this section, DPIV visualizations of the near wake of the model in two specific cases are provided in Fig. 12. The left column (plots a, c, e and g) are for the reference case without imposed rotation. The right column (plots b, d, f and h) are for a case where the amplitudes were largely reduced, with an amplitude of forced rotations of $\pi/4$ and a dimensionless forcing frequency of 1.5. In the right column, the cylinder has a double-sided arrow to indicate that this is the case with forced rotation. Both experiments were conducted at a reduced velocity of 6.2, where the largest amplitudes and the largest differences between the amplitudes of the nonrotating cylinder and the rotating one took place. The dimensionless vorticity ($\omega^* = \omega D/U$) data appear phase averaged at four positions in the oscillation cycle ($0, \pi/2, \pi$ and $3\pi/2$ rad), with the vorticity being ω . Each snapshot in the figures is the result of averaging more than 15 instantaneous vorticity maps in a field

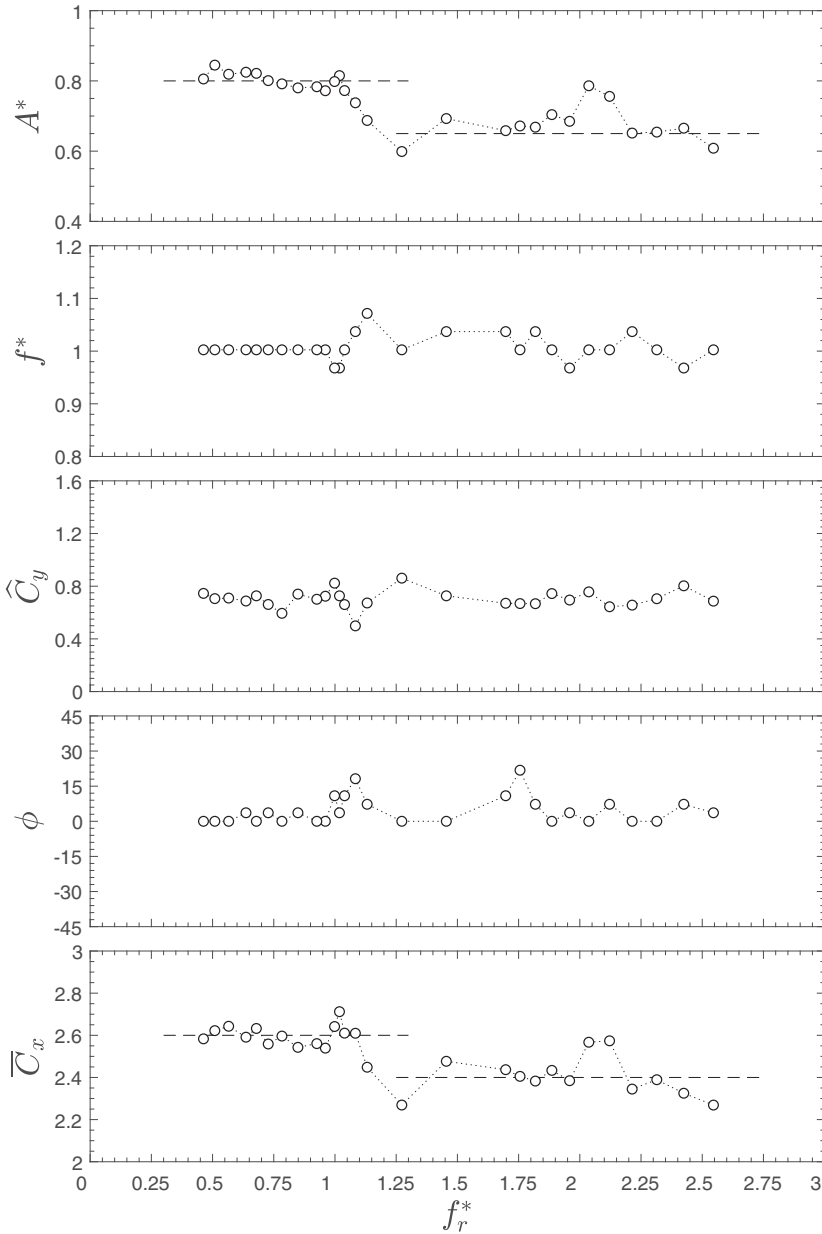


FIG. 11. Dimensionless amplitude (A^*), frequency (f^*), transverse force (\hat{C}_y), phase (ϕ), and in-line force (\bar{C}_x) as a function of dimensionless forced rotation frequency (f_r^*). All experiments were conducted at the same reduced velocity ($U^* \approx 6.2$).

of view that covers a region of more than 5×4 cylinder diameters around the rest position of the model.

Figure 12 clearly shows that the introduction of the forced rotation does not prevent the formation of the classical vortex street. A single vortex is shed at each side of the wake per cycle, with the wake having a similar topology when compared to the case without rotation. The minor differences that appear are related to the magnitude of the vorticity, which is diminished in the case of the forced

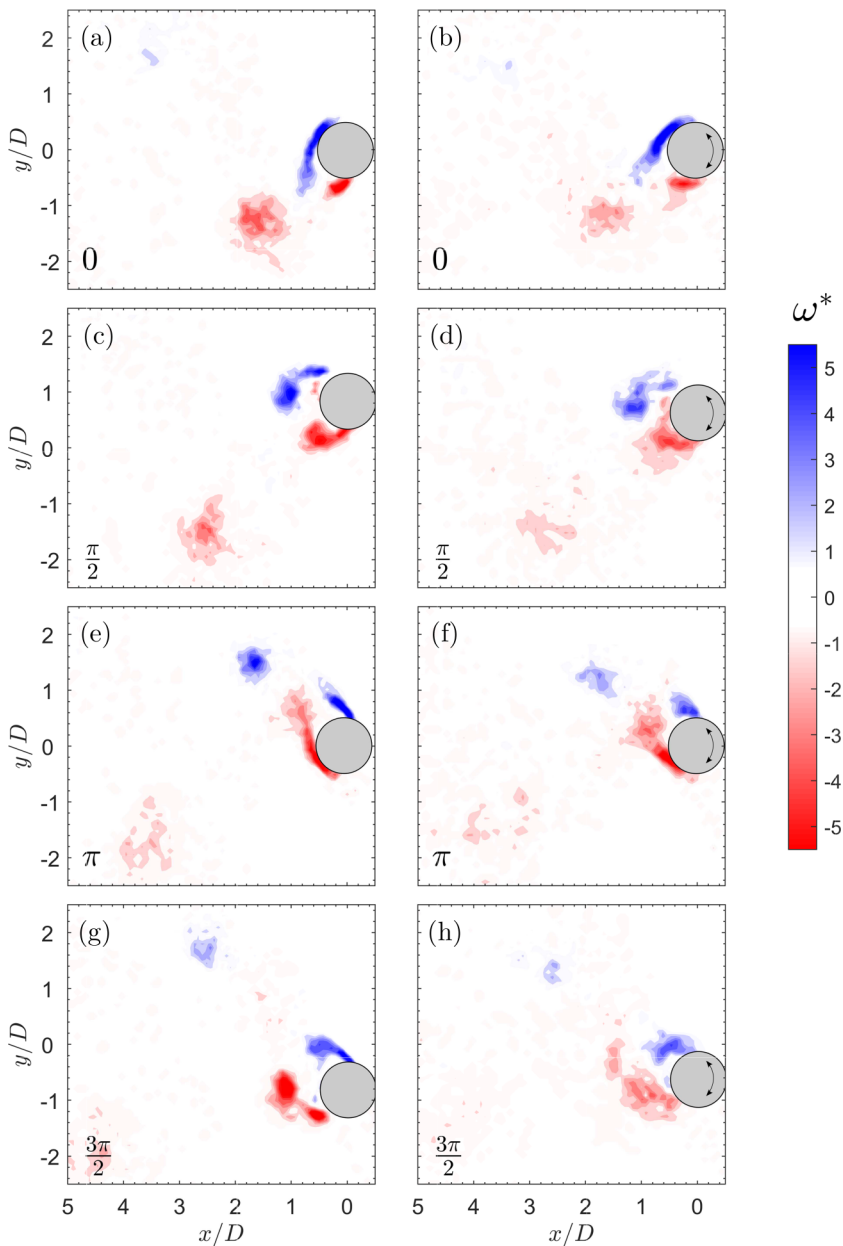


FIG. 12. Phase-averaged dimensionless vorticity fields at eight positions inside a VIV cycle, for the reference case (left column) and for a case with forced rotations with $f_r^* = 1.5$ and amplitude $\hat{\theta} = \pi/4$ rad (right column), both conducted at a $U^* \approx 6.2$.

rotation, leading to vortices that vanish faster than in the case with no rotation. The fact that the amplitude is reduced but the frequency is mostly not altered, as seen in Sec. III A, implies a smaller velocity of the cylinder that results in shear layers that detach from the cylinder with a smaller angle (Fig. 14), if compared to the nonrotating case (Fig. 13).

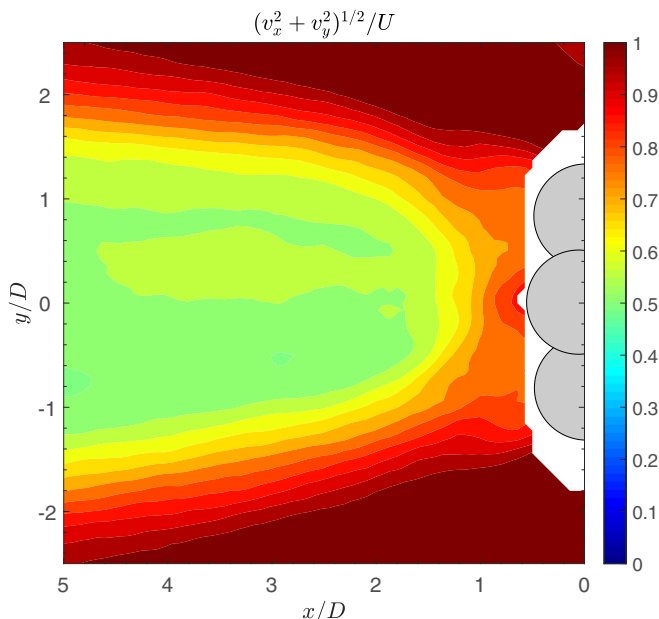


FIG. 13. Time-averaged dimensionless velocity field (magnitude) for the nonrotating cylinder case at a $U^* \approx 6.2$.

IV. DISCUSSION

The pioneering experimental work with a rotationally oscillating stationary cylinder conducted by Tokumaru and Dimotakis [35] described how substantial drag reductions could be achieved by applying rotational forcing to the cylinder. This fact made the authors suggest the possibility of reducing flow-induced vibrations using the same technique in cases with structures that are free to move. To the best knowledge of the author, there are no studies showing the effects of forced periodic rotations on VIVs that could answer their hypothesis. Their study was focused on describing the interactions between the vortex shedding and the rotational forcing applied to the stationary cylinder. They showed that the possibilities for flow control were most important when the forcing was synchronous to the shedding, and they concluded the process was governed by the injection of circulation into the separated flow region and its subsequent alteration. Although their experiments were done at considerably higher α , when compared to the ones in the present work (they did not have limitations on the size and mass of the auxiliary systems used to produce the rotations), the effects of the forcing suggested the same trends were valid at rates near the ones in the present work. Nevertheless, the self-sustained VIV motion of the cylinder poses a substantial difference, and after the present work, it seems that it dominates over the forcing, at least for the amplitude-frequency combinations reached here. In the present experiments we have seen a significant reduction of the dynamic response of the system for forcing frequencies slightly higher than the natural frequency, but even in these cases the near wake was not substantially altered when comparing it to the nonrotating case. The question remains completely unexplored for higher forcing frequencies.

Shiels and Leonard [37] tried to give a more detailed description of the causes for the drag reduction observations made by Tokumaru and Dimotakis [35], by conducting simulations with Re up to 15 000. The authors indicated how appropriate rotational oscillations of the cylinder were able to trigger circulation bursting in the boundary layers, resulting in the formation of multipole structures in the near wake of the cylinder. This ended up canceling part of the overall circulation,

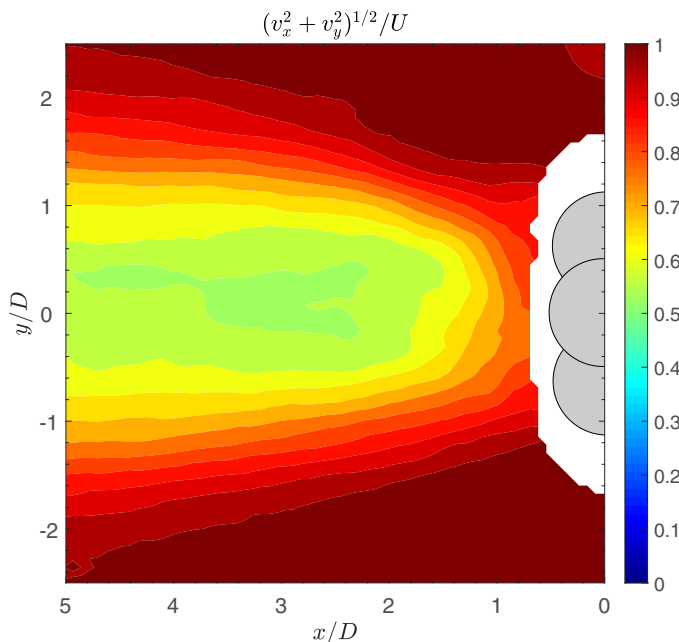


FIG. 14. Time-averaged dimensionless velocity field (magnitude), for the case with forced rotations of amplitude $\pi/4$ and dimensionless frequency of 1.5, at a $U^* \approx 6.2$.

preventing the growth of a large-scale recirculation region in the near wake, typical in nonrotating cylinders. This happened at rotational rates that are in the order of magnitude of those in the present work when rotation frequencies were near those at lock-in. The effect seems to be stronger as the rotational amplitude α gets larger and at high Re , otherwise it is diminished by viscosity. The numerical work by Choi *et al.* [33] pointed in the same direction. Our results and the DPIV data presented here show that if the cylinder is allowed to vibrate, the self-sustained oscillations dominate over the changes induced by the rotation, limiting their effects on the dynamics of the cylinder, at least for the forcing frequencies reached here. With the cylinder undergoing VIVs, the vortex strength increases, and therefore the rotary oscillations needed to induce circulation changes in the near wake in order to alter vortex formation need to be larger. The α values reached here might not have been large enough to promote the changes observed in the results by Shiels and Leonard [37] with their stationary cylinder.

More recent numerical simulations at low Re by Du and Dalton [34] were conducted with a rotationally oscillating stationary cylinder at rotating rates $\alpha = 0.5$ and 2 and frequencies f^* from 0 to 5, both similar to the ones used in the present experiments. They identified a clear influence on the vortex dynamics and force coefficients when the forcing frequency was near the shedding frequency or at higher harmonics, attributing it to a lock-in process between the vortices and the rotational forcing. At the smallest frequency that they studied they concluded that the influence of the forcing on the vortex shedding and hydrodynamic forces was very limited.

In the experiments presented here, with the cylinder undergoing VIVs, drag reduction took place at all rotational frequencies, associated with reductions in the motion amplitude, although significant changes in the wake have not been observed (Figs. 12–14). This indicates the changes in the circulation in the near wake produced by the forced periodic rotations were not important enough to trigger large changes in the wake. The circulation fed to the shear layers caused by the VIV motion is dominant over the forcing, at least for the values of α and frequencies deployed here. Nevertheless, as shown in Fig. 12, the forced rotation was able to weaken, in the phase-averaged sense, the vortices

that ended up dissipating faster. The change in phase from the in-phase to the out-of-phase condition takes place at smaller U^* (see Figs. 6 and 7), therefore the forced rotation promotes the reduction in amplitude as excitation opposes motion in a wider region of the response. Although in the present work it has been shown that VIV response can be modified using forced rotations, the question of how much VIV attenuation can be achieved by increasing forcing frequency or α remains partially unanswered due to the limitations imposed by the present experimental design.

V. CONCLUDING REMARKS

Experiments here show the effects of periodic rotational motions on the vortex-induced vibrations of a circular cylinder in cross-flow. Embedding all the actuators and sensors needed while keeping a low mass-damping imposed important design restrictions, as all these systems had to move with the cylinder. Although this was very challenging, the experimental setup has allowed the study of a wide parameter space with variations in Reynolds number in the range from approximately 9000 to 24 000 and reduced velocities from approximately 4.5 to 11. Two forcing rotational amplitudes of $\pi/6$ and $\pi/4$ with dimensionless forcing frequencies up to 2 were investigated, leading to velocity ratios α over 1.

For dimensionless frequencies smaller than 1, the rotary oscillations had little effect on the VIV response. Otherwise the dynamic response of the cylinder was reduced if compared to the nonrotating case, especially when forcing frequencies were larger than the VIV responding frequency under locked-in condition. Reductions of more than a 25% in amplitude were observed. Conversely, responding frequencies were not significantly altered by the forced rotation when compared to the nonrotating case. Even though vortex formation was dominated by the large-amplitude VIV motions as in nonrotating cylinders, the rotary oscillations induced an earlier change of the motion-excitation phase difference. Drag coefficients decreased because of the reduction in VIV amplitude, and the lift coefficient was reduced as well under lock-in conditions. The changes observed in the wake structures were minor, although vortices dissipated faster and showed smaller values of vorticity, all indicating that the VIV motion dominated the vortex formation process as in nonrotating cylinders instead of the rotary oscillations. The large changes in the wake topology observed by other researchers with rotationally oscillating stationary cylinders have not been observed in the present case. Nevertheless, these questions remain completely unexplored for cases with higher frequency forcing.

ACKNOWLEDGMENTS

The author would like to acknowledge the funding provided by Agència de Gestió d'Ajuts Universitaris i de Recerca (AGAUR) through grant 2017 SGR 1263 and by the Agencia Estatal de Investigación (AEI) through grant 2019 PGC2018-097766-B-I00.

-
- [1] M. M. Zdravkovich, *Flow around Cylindrical Structures, vol. 1, Fundamentals* (Oxford University Press, 1997).
 - [2] P. W. Bearman, Vortex shedding from oscillating bluff bodies, *Annu. Rev. Fluid Mech.* **16**, 195 (1984).
 - [3] C. H. K. Williamson, Vortex dynamics in the cylinder wake, *Annu. Rev. Fluid Mech.* **28**, 477 (1996).
 - [4] C. H. K. Williamson and R. Govardhan, Vortex-induced vibrations, *Annu. Rev. Fluid Mech.* **36**, 413 (2004).
 - [5] T. Sarpkaya, A critical review of the intrinsic nature of vortex-induced vibrations, *J. Fluids Struct.* **19**, 389 (2004).
 - [6] C. H. K. Williamson and R. Govardhan, A brief review of recent results in vortex-induced vibrations, *J. Wind Eng. Ind. Aerodyn.* **96**, 713 (2008).
 - [7] P. W. Bearman, Circular cylinder wakes and vortex-induced vibrations, *J. Fluids Struct.* **27**, 648 (2011).

-
- [8] R. D. Blevins, *Flow-Induced Vibration*, 2nd ed. (Van Nostrand Reinhold, 1990).
- [9] E. Naudascher and D. Rockwell, *Flow-Induced Vibrations. An Engineering Guide* (A. A. Balkema, 1994).
- [10] B. M. Sumer and J. Fredsoe, *Hydrodynamics around Cylindrical Structures*, 2nd ed. (World Scientific, Singapore, 1997).
- [11] M. P. Paidoussis, S. J. Price, and E. De Langre, *Fluid-Structure Interactions: Cross-flow-Induced Instabilities* (Cambridge University Press, New York, 2010).
- [12] F. Díaz, J. Gavalda, J. G. Kawai, J. F. Keffer, and F. Giralt, Vortex shedding from a spinning cylinder, *Phys. Fluids* **26**, 3454 (1983).
- [13] F. Diaz, J. Gavalda, J. G. Kawai, J. F. Keffer, and F. Giralt, Asymmetrical wake generated by a spinning cylinder, *AIAA J.* **23**, 49 (1985).
- [14] Y. T. Chew, M. Cheng, and S. C. Luo, A numerical study of flow past a rotating circular cylinder using a hybrid vortex scheme, *J. Fluid Mech.* **299**, 35 (1995).
- [15] S. Mittal, Three-dimensional instabilities in flow past a rotating cylinder, *Trans. ASME: J. Appl. Mech.* **71**, 89 (2004).
- [16] R. El Akoury, M. Braza, R. Perrin, G. Harran, and Y. Hoarau, The three-dimensional transition in the flow around a rotating cylinder, *J. Fluid Mech.* **607**, 1 (2008).
- [17] S. Kumar, C. Cantu, and B. Gonzalez, Flow past a rotating cylinder at low and high rotation rates, *Trans. ASME: J. Fluids Eng.* **133**, 41201 (2011).
- [18] A. Radi, M. C. Thompson, A. Rao, K. Hourigan, and J. Sheridan, Experimental evidence of new three-dimensional modes in the wake of a rotating cylinder, *J. Fluid Mech.* **734**, 567 (2013).
- [19] A. Rao, A. Radi, J. S. Leontini, M. C. Thompson, J. Sheridan, and K. Hourigan, A review of rotating cylinder wake transitions, *J. Fluids Struct.* **53**, 2 (2015).
- [20] P. K. Stansby and R. C. T. Rainey, On the orbital response of a rotating cylinder in a current, *J. Fluid Mech.* **439**, 87 (2001).
- [21] P. K. Stansby and R. C. T. Rainey, A CFD study of the dynamic response of a rotating cylinder in a current, *J. Fluids Struct.* **15**, 513 (2001).
- [22] R. Bourguet and D. Lo Jacono, Flow-induced vibrations of a rotating cylinder, *J. Fluid Mech.* **740**, 342 (2014).
- [23] R. Bourguet, Flow-induced vibrations of a rotating cylinder in an arbitrary direction, *J. Fluid Mech.* **860**, 739 (2019).
- [24] M. Zhao, L. Cheng, and L. Lu, Vortex induced vibrations of a rotating circular cylinder at low Reynolds number, *Phys. Fluids* **26**, 073602 (2014).
- [25] J. Zhao, D. Lo Jacono, J. Sheridan, K. Hourigan, and M. C. Thompson, Experimental investigation of in-line flow-induced vibration of a rotating circular cylinder, *J. Fluid Mech.* **847**, 664 (2018).
- [26] B. Seyed-Aghazadeh and Y. Modarres-Sadeghi, An experimental investigation of vortex-induced vibration of a rotating circular cylinder in the crossflow direction, *Phys. Fluids* **27**, 067101 (2015).
- [27] Rémi Bourguet and D. Lo Jacono, In-line flow-induced vibrations of a rotating cylinder, *J. Fluid Mech.* **781**, 127 (2015).
- [28] K. W. L. Wong, J. Zhao, D. L. Jacono, and M. C. Thompson, Experimental investigation of flow-induced vibration of a rotating circular cylinder, *J. Fluid Mech.* **829**, 486 (2017).
- [29] F. J. Huera-Huarte and A. Vernet, Vortex modes in the wake of an oscillating long flexible cylinder combining POD and fuzzy clustering, *Exp. Fluids* **48**, 999 (2010).
- [30] M. H. Chou, Synchronization of vortex shedding from a cylinder under rotary oscillation, *Comput. Fluids* **26**, 755 (1997).
- [31] N. Fujisawa, K. Ikemoto, and K. Nagaya, Vortex shedding resonance from a rotationally oscillating cylinder, *J. Fluids Struct.* **12**, 1041 (1998).
- [32] M. H. Chou, Numerical study of vortex shedding from a rotating cylinder immersed in a uniform flow field, *Int. J. Numer. Methods Fluids* **32**, 545 (2000).
- [33] S. Choi, H. Choi, and S. Kang, Characteristics of flow over a rotationally oscillating cylinder at low Reynolds number, *Phys. Fluids* **14**, 2767 (2002).
- [34] L. Du and C. Dalton, LES calculation for uniform flow past a rotationally oscillating cylinder, *J. Fluids Struct.* **42**, 40 (2013).

- [35] P. T. Tokumaru and P. E. Dimotakis, Rotary oscillation control of a cylinder wake, *J. Fluid Mech.* **224**, 77 (1991).
- [36] P. T. Tokumaru and P. E. Dimotakis, The lift of a cylinder executing rotary motions in a uniform flow, *J. Fluid Mech.* **255**, 1 (1993).
- [37] D. Shiels and A. Leonard, Investigation of a drag reduction on a circular cylinder in rotary oscillation, *J. Fluid Mech.* **431**, 297 (2001).
- [38] F. J. Huera-Huarte, Dynamics and excitation in a low mass-damping cylinder in cross-flow with side-by-side interference, *J. Fluid Mech.* **850**, 370 (2018).
- [39] F. J. Huera-Huarte, Suppression of vortex-induced vibration in low mass-damping circular cylinders using wire meshes, *Mar. Struct.* **55**, 200 (2017).
- [40] J. I. Jiménez-González and F. J. Huera-Huarte, Experimental sensitivity of vortex-induced vibrations to localized wake perturbations, *J. Fluids Struct.* **74**, 53 (2017).
- [41] A. Khalak and C. H. K. Williamson, Motions, forces and mode transitions in vortex-induced vibrations at low mass-damping, *J. Fluids Struct.* **13**, 813 (1999).